Frequency Domain Reverse Time Migration of GPR with Attenenuation Compensation

Hai Liu, Bangan Xing, Feng Han
Institute of Electromagnetics and Acoustics
Xiamen University
Xiamen 361005, China
Email: liuhai8619@xmu.edu.cn

Feng Zhou
School of Mechanical Engineering and Electronic Information
China University of Geosciences (Wuhan)
Wuhan 430074, China

Abstract—**High computational cost is always a critical concern for reverse-time migration (RTM), and prevents its applications to ground penetrating radar (GPR). To address this challenge, a frequency domain RTM algorithm based on the layered medium dyadic Green's function (DGF) is proposed for high-resolution and efficient subsurface imaging using GPR. To mitigate the amplitude distortion in lossy media, the attenuation compensation in the backward wavefield extrapolation is performed by modifying the computation of DGFs in layered media. The final image is reconstructed by the direct summation of all the wavefields for all the sampling frequencies in the frequency domain, instead of transforming them back to the time domain and processing them. Both numerical and laboratory experiments are conducted to verify the performance of the proposed algorithm, and the results show that our algorithm can yield almost the same subsurface image with the conventional time domain RTM algorithm, but requires less than two orders of magnitude in computational costs. The results also show that the quality of the RTM image in the conductive background medium can be significantly enhanced by compensating the wave attenuation.**

Keywords—Ground penetrating radar (GPR); reverse time migration (RTM); layered medium Green's function; attenuation compensation

I. INTRODUCTION

As an efficient and high-resolution subsurface sensing tool, ground penetrating radar (GPR) has been widely applied in various fields, such as environmental studies [1], hydrological monitoring [2], non-destructive testing of civil engineering structures [3-5], planet exploration [6], and landmine detection [7], etc. Conventionally, Migration is applied to GPR data acquired in these applications to obtain a focused image of the subsurface reflectivity of electromagnetic waves, which illustrates the object's true location and size. Various migration algorithms, such as Kirchhoff migration, diffraction stacking, and phase-shift migration, have been used in reconstructing the GPR images.

Reverse time migration (RTM) is based on the two-way wave equation and can be viewed as the matched filtering between the incident field and the time-reversed receiver field [8]. Because it possesses high accuracy in reconstructing images of subsurface complex structures, RTM has become a routine imaging technique for the seismic exploration [9], and has also been applied to GPR imaging [10] in recent years. The finite-difference time domain (FDTD) method is conventionally used to calculate the wavefields during the forward and backward extrapolations in RTM. This makes RTM computationally expensive and even impractical, when huge amount of GPR data is acquired during high-speed surveys. Besides, the energy loss of the radar signal propagating in the subsurface medium is much more severe than that of seismic waves. Therefore, we have to consider the wave attenuation caused by the electric conductivity in the background media is for RTM of GPR [11].

In this paper, we propose a frequency-domain RTM algorithm utilizing the dyadic Greens function (DGF) in layered media [12], which can greatly enhance the computational efficiency. Both the forward and backward extrapolation wavefields in the imaging region are computed by the multiplication between the frequency spectra of the excitation sources and the layered medium DGFs. In order to compensate the intrinsic attenuation in the backward wavefield extrapolation, we modify the evaluation of DGFs by reversing the sign of the imaginary part of the wave vector $\boldsymbol{k}$ in the spectrum domain before the Sommerfeld integration is taken. Meanwhile, the evanescent wave is omitted due to its negligible contribution to the RTM image. The final image is reconstructed by multiplication of the source and receiver wavefields in the frequency domain. To evaluate the performance and efficiency of our frequency-domain RTM (FRTM) algorithm for GPR imaging, we conducted both numerical and laboratory experiments, and compare the consumption of computation time and memory between the FRTM algorithm based on the DGFs and the conventional time-domain RTM (TRTM) algorithm based on the FDTD method.

II. METHODS

A. FRTM Algorithm

Forward propagation of the source wavefield, backward propagation of the receiver wavefield, and imaging condition are three main steps of the algorithm of RTM. According to our algorithm, both the forward and backward wavefield extrapolation are employed in this frequency domain. The expressions of the spectra of the wavefields are given by [13]

$$\mathbf{U}_s(\mathbf{r}, \omega) = \overline{\overline{\mathbf{G}}}(\mathbf{r}, r_s, \omega) \cdot \mathbf{S}(r_s, \omega) \tag{1}$$

$$\mathbf{U_r}(\mathbf{r}, \omega) = \bar{\bar{\mathbf{G}}}(\mathbf{r}, r_r, \omega) \cdot \mathbf{R}^*(r_r, \omega) e^{-j\omega T} \qquad (2)$$

where $U_s(\mathbf{r}, \omega)$ and $U_r(\mathbf{r}, \omega)$ are the Fourier transformation of the source wavefield and receiver wavefield, $\bar{\bar{\mathbf{G}}}$ is the DFG, $\mathbf{S}(r_s, \omega)$ is the spectra of the source waveform excited at the source location r_s, and $\mathbf{R}^*(r_r, \omega)$ is complex conjugate of the spectra of the recorded GPR trace at the receiver location r_r. The DFG is a second order tensor for each frequency at each grid in the imaging domain, which can be written as

$$\bar{\bar{\mathbf{G}}}(\mathbf{r}, r_s, \omega) =$$

$$\begin{bmatrix} g_{xx}(\mathbf{r}, r_s, \omega) & g_{xy}(\mathbf{r}, r_s, \omega) & g_{xz}(\mathbf{r}, r_s, \omega) \\ g_{yx}(\mathbf{r}, r_s, \omega) & g_{yy}(\mathbf{r}, r_s, \omega) & g_{yz}(\mathbf{r}, r_s, \omega) \\ g_{zx}(\mathbf{r}, r_s, \omega) & g_{zy}(\mathbf{r}, r_s, \omega) & g_{zz}(\mathbf{r}, r_s, \omega) \end{bmatrix} \qquad (3)$$

Due to GPR usually works in a perpendicular broadside mode and uses linearly-polarized antennas for transmission and reception, only one component of the dyad $\bar{\bar{\mathbf{G}}}$, e.g. $g_{yy}(\mathbf{r}, r_s, \omega)$ or $g_{yy}(\mathbf{r}, r_r, \omega)$, needs to be evaluated for computing spectra of the wavefields.

The computation cost can be drastically reduced by virtue of the property of symmetry and horizontal translation-invariance of the DGF. Furthermore, the g_{yy} of $\bar{\bar{\mathbf{G}}}(\mathbf{r}, r_s, \omega)$ can be accelerated by the Chebyshev interpolation in a horizontal plane and it can be expressed as

$$g_{yy}(\mathbf{r}, r_s, \omega) = g_{yy}(\rho, z, z_s, \omega)$$

$$= g'_{yy}(\rho, z, z_s, \omega) f(\varphi) \qquad (4)$$

where $\rho = \sqrt{(x - x_s)^2 + (y - y_s)^2}$, $\cos\varphi = \frac{x - x_s}{\rho}$, $\sin\varphi = \frac{y - y_s}{\rho}$, and $f(\varphi)$ is a function of the azimuth angle φ.

Fig. 1. The Sommerfeld integration path of k_ρ (red line) for the computation of DGFs. (a) When the electric conductivity is positive. (b) When the electric conductivity is negative.

The imaging condition in the frequency domain is realized by calculating the zero-lag cross correlation of the source and receiver wavefields, which can be written as

$$I(\mathbf{r}) = \frac{1}{2\pi} \int_{-\infty}^{\infty} U_s(\mathbf{r}, \omega) \, U_r(\mathbf{r}, \omega) e^{-j\omega T} d\omega \qquad (5)$$

where $I(\mathbf{r})$ is the reconstructed image generated from a common-source GPR gather and T is the time window of the recorded GPR traces.

B. Plane Wave Attenuation Caused by Electric Conductivity

The plane wave attenuation in conductive media is discussed at first before explaining our attenuation compensating method.

The wave vector of plane wave can be written as

$$\mathbf{k} = \hat{\mathbf{k}}\omega\sqrt{\mu_0\epsilon} = \hat{\mathbf{k}}(\beta - j\alpha) \qquad (6)$$

where

$$\beta = \omega\sqrt{\mu_0\epsilon}\sqrt{\frac{1}{2}\left(\sqrt{1 + \left(\frac{\sigma}{\omega\epsilon}\right)^2} + 1\right)} \qquad (7)$$

is the propagation factor, and

$$\alpha = \text{sgn}(\sigma)\omega\sqrt{\mu_0\epsilon}\sqrt{\frac{1}{2}\left(\sqrt{1 + \left(\frac{\sigma}{\omega\epsilon}\right)^2} - 1\right)} \qquad (8)$$
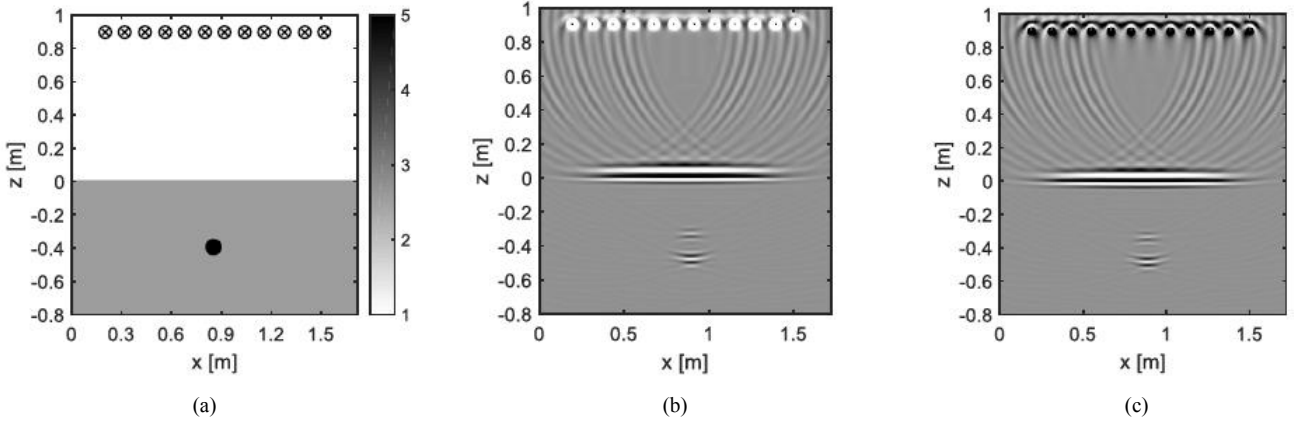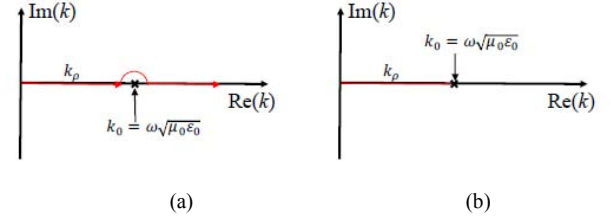

Fig. 2. Comparison between the 2D imaging results obtained by (b) the conventional TRTM and (c) the proposed FRTM using a synthetic MIMO GPR dataset from (a) the numerical model. A cylinder rock object with a radius of 5 cm is buried in the subsurface regolith.

TABLE I. COMPARISONS OF THE COMPUTATION CONSUMPTION BETWEEN TRTM AND FRTM FOR THE 2D MIMO GPR NUMBERICAL EXPERIMENT

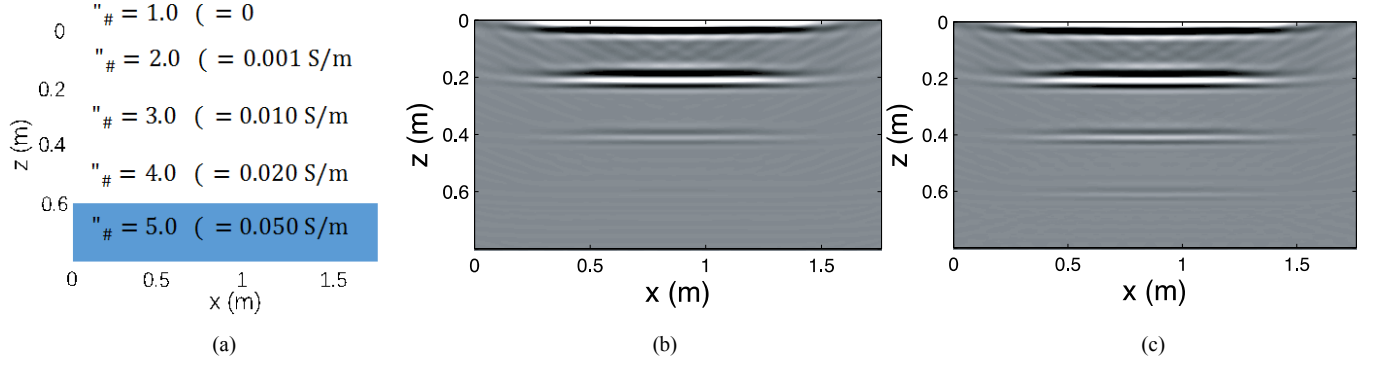|		CPU cores/threads	Memory (MB)	Time (s)
FRTM	DGF computation	24/48	40	3380
	DGF interpolation	1/1	20	8
	RTM imaging			17
TRTM	RTM imaging	1/1	1400	10800

Fig. 3. Comparison of the 2D imaging results of FRTM without and with the attenuation compensation. (a) The numerical model. (b) Image without attenuation compensation. (c) Image with attenuation compensation. Images are displayed in the same scale.

is the attenuation factor, ω is angular frequency, ε is the permittivity of the medium is, μ_0 is the permeability of air and σ is the electric conductivity, the symbol sgn represents the sign function. A positive α and a negative α will cause the EM energy decaying in the propagation and the EM energy growing in the propagation, respectively. Since the sign of α has no effect on the propagation factor, the phase velocity keeps unchanged if the electric conductivity becomes negative. Only the amplitude of the plane wave increases. So, it is convenient to change the wave vector k to its complex conjugate to compute the plane wavefield in a medium with a negative electric conductivity.

C. Attenuation Compensation for RTM by Modifying DGFs

Since the FRTM of GPR data is based on layered medium DGFs which are computed by decomposing the spherical wave into a series of plane waves and taking a Sommerfeld integration later, it is straightforward to compensate each plane wave component in the spectrum domain by changing the wave vector **k** to its complex conjugate for the backward extrapolation.

The wave vector of the EM wavefield extrapolated form both the transmitters and receivers is $\mathbf{k} = \hat{\mathbf{k}}\omega\sqrt{\mu_0\epsilon}$. If we define the z axis downward and is perpendicular to the layer boundaries, the z component of the wave vector is $k_z = \sqrt{k_0{}^2 - k_\rho{}^2}$, where $k_\rho = \sqrt{k_x{}^2 - k_y{}^2}$. When the DGFs are evaluated, the integration path of k_ρ should follow the red line shown in Fig. 1(a). The arc is used to bypass the singularity of the integration. Before the FRTM is executed, the layered medium DGFs are first evaluated through the Sommerfeld integration. This numerical integration actually cannot converge if k_ρ extends to infinity. In order to obtain stable DGFs for RTM attenuation compensation, we just discard the evanescent wave mentioned above and let the integration path of k_ρ follows the red line shown in Fig1(b). This is reasonable since the contribution of the evanescent wave to DGFs is negligible compared with that from the normally downward propagating wave.

III. NUMBERICAL EXPERIMENTS

To validate the proposed FRTM algorithm, a simulation experiment configured with twelve antennas (point sources) is conducted and the simulated model is shown in Fig. 2(a). The relative dielectric permittivity of the regolith and the larva rock are set to be 2.5 and 5, respectively, and the electric conductivity are 10^{-5} S/m and 10^{-4} S/m, respectively. Twelve antennas (point sources) are used as a transmitting antenna in turn and the other eleven antennas are used as receiving
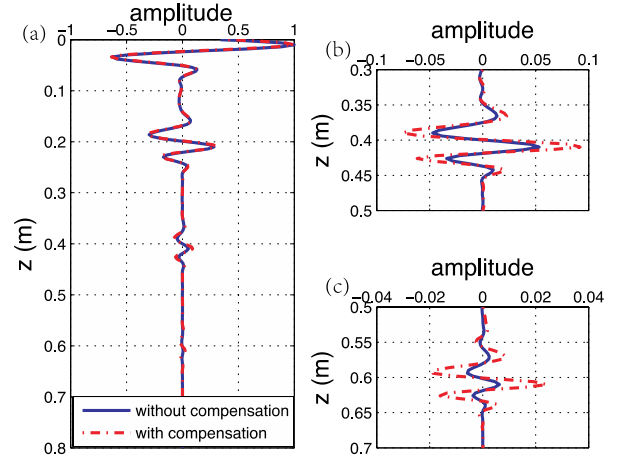

Fig. 4. Comparisons of the traces (at x = 0.9 m) without and with attenuation compensation. The amplitudes are normalized with the same factor. (a) the whole trace. (b) and (c) are the zoom-in figures for the boundary at z = 0.4 m and z = 0.6 m, respectively.

antennas, and thus 132 synthetic GPR traces are obtained by twelve FDTD simulations.

Fig. 2(b) and 2(c) show the 2D images reconstructed by TRTM and FRTM using a half-space initial model, respectively. No difference can be discerned between the two reconstructed images except the phase difference at the source locations, which can be explained by the fact that the electric fields in the region very close to the source point cannot be accurately simulated by the FDTD method. The computation resources consumed by the two RTM algorithms are given in table I. The FRTM algorithm consumes less than one fiftieth of the memory and one percent of the computation time cost by the TRTM algorithm.

Now, let us verify the attenuation compensation algorithm in RTM. We use the same antenna array configuration as in last case but divide the underground region into four layers. Each layer has its own permittivity and conductivity, as is shown in Fig. 3(a). The conductivity increases as the depth increases. Fig. 3(b) and 3(c) show the RTM image without and with attenuation compensation, respectively. It should be noted that two figures are displayed in the same scale. Clearly, the boundary at z = 0.4 m obtains an improved illumination after compensation. The boundary at z = 0.6 m is almost not discernable without compensation but properly recovered with the conductivity attenuation compensation.
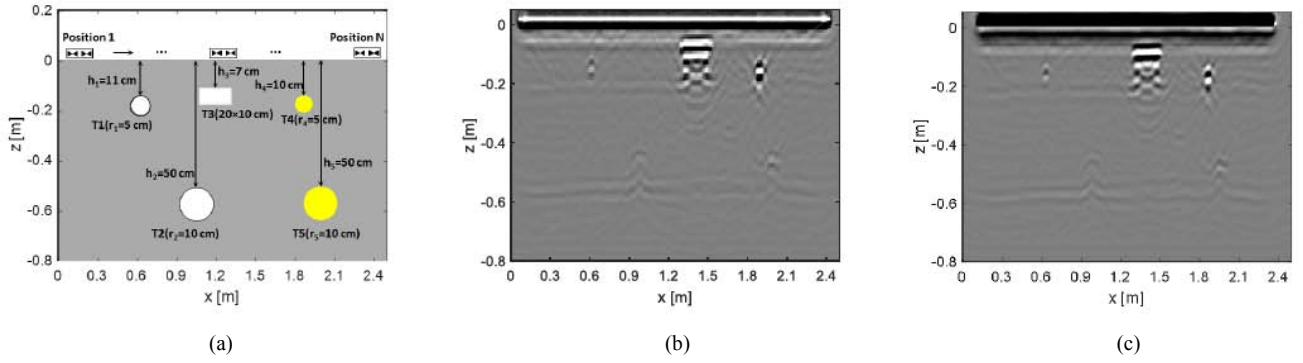
Fig. 5. Comparison between the 2D imaging results obtained by (b) the conventional TRTM and (c) the proposed FRTM using a measured CO GPR profile from (a) the experimental model. The two air-filled plastic pipes (marked by T1 and T2) and one air-filled glass cube (marked by T3) are marked by white color and two metal pipes (marked by T4 and T5) are marked by yellow color.

Fig. 4 shows the traces at $x = 0.9$ m. We can see that the discrepancy between the RTM results without compensation and with compensation becomes larger when the boundary is deeper. This is because the the conductivity is larger for deeper boundaries. The electromagnetic energy loss is more obvious for the deeper boundaries and thus the compensation is also more obvious.

IV. LABORATORY EXPERIMENTS

The results of laboratory experiments are presented in this section. As shown in Fig. 5(a), a common offset (CO) GPR profile containing 533 traces with a step of 4 mm was recorded over a sandpit by a commercial GPR system with the center frequency of 1.6 GHz. A half-space initial model is used for both the TRTM and FRTM algorithms. The relative dielectric permittivity and electric conductivity of the sand are set to be 3.0 and 0.1 mS/m, respectively. The source wavelet for RTM was recorded from a reflection from a metal plate buried at a depth of about 30 cm in the sand. As shown in Fig. 5(b) and 5(c), the 2D subsurface images reconstructed by the TRTM and FRTM are almost the same. The CPU cores and threads are same as that in numberical experiments. For FRTM, DGF computation costs 50MB in memory and 34800s in time, DGF interpolation and RTM imaging cost 40MB in memory totally and 61s and 373s in time respectively. As contrast, RTM imaging costs 2500MB in memory and 679000s in time for TRTM. Since the TRTM algorithm has to run two FDTD simulations for each source location, it consumes a computation time of about eight days, which is unaffordable for real GPR applications. While the FRTM algorithm needs calculating the DFGs only once, it consumes about ten hours, one minute and six minutes for the DFG computation, DFG interpolation and the RTM imaging, respectively. The remarkable reduction in the memory and computation time by a magnitude of two orders is a great advantage of the proposed FRTM algorithm.

V. CONLUSIONS

A FRTM algorithm based on the layered medium DFG has been presented in this paper. Through the results of the one numerical and the two laboratory experiments, it is concluded that the FRTM can reconstruct the same subsurface image as the conventional TRTM based on the FDTD method. The DFGs of the layered media need to be calculated only once due to its property of translation-invariance and symmetry in the horizontal plane. Moreover, since DFGs can be computed and saved in disk in advance, the imaging time required by the FRTM algorithm can be drastically reduced to less than a

magnitude of two orders, compared with that of the TRTM. Comparison of the simulation results of image with and without attenuation compensation shows this newly proposed compensation algorithm can handle the energy attenuation in RTM efficiently.

REFERENCES

[1] H. Liu, K. Takahashi, and M. Sato, "Measurement of dielectric permittivity and thickness of snow and ice on a brackish lagoon using GPR," *IEEE J. Sel. Top. Appl. Earth Obs. Remote Sens.*, vol. 7, no. 3, pp. 820–827, 2014.

[2] H. Liu, X. Xie, J. Cui, K. Takahashi, and M. Sato, "Groundwater level monitoring for hydraulic characterization of an unconfined aquifer by common mid-point measurements using GPR," Journal of Environmental and Engineering Geophysics, vol. 19, no. 4, pp. 259–268, Dec. 2014.

[3] H. Liu and M. Sato, "In situ measurement of pavement thickness and dielectric permittivity by GPR using an antenna array," *NDT&E Int.*, vol. 64, no. June, pp. 65–71, 2014.

[4] H. Liu, Z. Deng, F. Han, Y. Xia, Q. H. Liu, and M. Sato, "Time-frequency analysis of air-coupled GPR data for identification of delamination between pavement layers," *Constr. Build. Mater.*, vol. 154, pp. 1207–1215, 2017.

[5] H. Liu, C. Koyama, J. Zhu, Q. Liu, and M. Sato, "Post-Earthquake Damage Inspection of Wood-Frame Buildings by a Polarimetric GB-SAR System," *Remote Sens.*, vol. 8, no. 11, p. 935, 2016.

[6] L. Xiao, P. Zhu, and G. Fang, "A young multilayered terrane of the northern Mare Imbrium revealed by Chang' E-3 mission," Science, vol. 347, pp. 1226–1229, 2015.

[7] X. Feng, M. Sato, and C. Liu, "Hand-held GPR imaging using migration for irregular data," IEEE J. Sel. Top. Appl. Earth Obs. Remote Sens., vol. 4, no. 4, pp. 799–803, Dec. 2011.

[8] C. J. Leuschen and R. G. Plumb, "A matched-filter-based reverse-time migration algorithm for ground-penetrating radar data," IEEE Trans. Geosci. Remote Sens., vol. 39, no. 5, pp. 929–936, May 2001.

[9] H. Liu, Z. Long, B. Tian, F. Han, G. Fang, and Q. H. Liu, "Two-Dimensional Reverse-Time Migration Applied to GPR with a 3-D-to-2-D Data Conversion," *IEEE J. Sel. Top. Appl. Earth Obs. Remote Sens.*, vol. 10, no. 10, pp. 4313–4320, 2017.

[10] J. Xie, Z. Guo, H. Liu, and Q. H. Liu, "Reverse Time Migration Using the Pseudospectral Time-Domain Algorithm," *J. Comput. Acoust.*, vol. 24, no. 2, p. 1650005, 2016.

[11] H. Liu, Z. Long, B. Tian, F. Han, G. Fang, and Q. H. Liu, "TwoDimensional Reverse-Time Migration Applied to GPR With a 3-D-to-2D Data Conversion," IEEE J. Sel. Top. Appl. Earth Obs. Remote Sens., vol. 10, no. 10, pp. 4313–4320, 2017.

[12] T. Zhu, J. M. Carcione, and M. A. B. Botelho, "Reverse time imaging of ground-penetrating radar and SH-seismic data including the effects of wave loss," Geophysics, vol. 81, no. 4, pp. H21–H32, 2016.

[13] H. Liu, D. Z., H. F., Y. Xia, Q. H. Liu, and S. M., "Time-frequency analysis of air-coupled GPR data for identification of delamination between pavement layers," Constr. Build. Mater., vol. 154, pp. 1207–1215, 2017.